

Optimizing the Performance of Printed Indium Oxide Thin-Film Transistors through Gallium Incorporation

Mahsa K. Saghafi, Mohana Veerraju Kante, Ramin Shadkam, Evgeniy Boltynjuk, Simon Schweidler, Ben Breitung, Michael Hirtz, Jasmin Aghassi-Hagmann,* and Gabriel Cadilha Marques*

The present study explores the optimization of printed electrolyte-gated field-effect transistors (EGTs) with an indium oxide ($\text{In}_2\text{O}_{3-x}$) channel by introducing gallium into the $\text{In}_2\text{O}_{3-x}$ material. Indium oxide ($\text{In}_2\text{O}_{3-x}$) and indium gallium oxide (IGO) nanoparticles are synthesized and formulated into water-based functional inks for printing $\text{In}_2\text{O}_{3-x}$ and IGO thin films at room temperature. These thin films are characterized and employed as the semiconductor channel for EGTs. Gallium incorporation shifts the EGT threshold voltage from 0.2 to 0.5 V and reduces the off-current by up to three orders of magnitude depending on the gallium concentration. Shifting the threshold voltage toward positive values while reducing off-currents is essential for designing logic gates in various topologies, such as transistor-resistor logic and transistor-transistor logic, as demonstrated in inverter structures. Prepared inverters using IGO exhibit slightly higher gain and lower power consumption.

1. Introduction

Metal-oxide-based semiconductors are widely used in various applications due to their high carrier density and carrier mobility.^[1] Among these, indium oxide ($\text{In}_2\text{O}_{3-x}$) stands out as a channel material in accumulation-mode n-type thin-film transistors (TFTs), due to the possibility of utilizing both vacuum^[2–4] and solution-based^[5] processes for preparation. This compatibility facilitates the integration of indium oxide precursors with printing techniques, such as inkjet printing, for fabricating TFTs.^[6] However, the high

calcination temperatures ($>500^\circ\text{C}$) required to form indium oxide thin films limit the choice of substrates.^[7] Conversely, indium oxide nanoparticle inks have demonstrated the ability to reduce curing temperatures to around 100°C , although this temperature decrease is often at the expense of performance.^[8,9] Regardless of the deposition technique and thermal curing conditions, the high carrier density in indium oxide thin films, which makes the material promising for electronic applications, is primarily attributed to oxygen vacancies within the crystal structure.^[10,11]

Oxygen vacancies, one of the most common defects in metal oxides, create localized electronic states that can act as free charge carriers within the crystal structure. The number of these defects depends on


the material's nature, fabrication methods, and presence of dopants.^[12] In n-type TFTs, an excessive number of free electrons can cause the threshold voltage (V_{th}) to shift toward negative values, requiring a lower or even negative gate potential to turn the device off.^[13,14] While TFTs with a negative threshold voltage operate in depletion mode, enhancement-mode TFTs are generally preferred for circuit design due to their more stable off-state control. However, some enhancement-mode TFTs may still exhibit high leakage currents at a gate-source bias of 0 V, where the TFT should ideally be off, leading to increased power consumption in microelectronic circuits.

Reducing the concentration of oxygen vacancies is a viable approach to achieve enhancement-mode operation with moderate leakage currents in indium oxide-channel TFTs. Dopants that can bind to oxygen have the potential to decrease the number of vacancies within the indium oxide crystal structure. However, reducing oxygen vacancies may also lower the on-currents, requiring careful optimization to balance between on-currents, off-currents, and threshold voltage.

The extent to which the doping shifts the threshold voltage in a TFT depends heavily on the choice of gate-insulator material and the processing steps of the indium oxide thin films. Tungsten (W) is a dopant commonly used with indium oxide to enhance the electrical performance of TFTs by suppressing excess oxygen vacancies and reducing the free electron concentration. Optimized W concentrations improve the on-current and $I_{\text{on}}/I_{\text{off}}$ ratios. While moderate W doping does not induce a significant shift in the average threshold voltage, as demonstrated in

M. K. Saghafi, M. Veerraju Kante, R. Shadkam, E. Boltynjuk, S. Schweidler, B. Breitung, M. Hirtz, J. Aghassi-Hagmann, G. Cadilha Marques
Institute of Nanotechnology (INT)
Karlsruhe Institute of Technology (KIT)
Kaiserstraße 12, 76131 Karlsruhe, Germany
E-mail: jasmin.aghassi@kit.edu; gabriel.marques@kit.edu

M. K. Saghafi, M. Hirtz
Karlsruhe Nano Micro Facility (KNMF)
Karlsruhe Institute of Technology (KIT)
Kaiserstraße 12, 76131 Karlsruhe, Germany

 The ORCID identification number(s) for the author(s) of this article can be found under <https://doi.org/10.1002/pssa.202500294>.

© 2025 The Author(s). physica status solidi (a) applications and materials science published by Wiley-VCH GmbH. This is an open access article under the terms of the Creative Commons Attribution License, which permits use, distribution and reproduction in any medium, provided the original work is properly cited.

DOI: 10.1002/pssa.202500294

TFTs with spin-coated W-doped indium oxide channels and Al_2O_3 gate-insulators, it notably enhances the reproducibility of V_{th} . However, at higher doping levels, the threshold voltage may shift to positive values, while the on/off ratio significantly decreases. Excess W can also create charge traps, further deteriorating TFT performance.^[15] Besides W, Ytterbium (Yb) has also been used to dope indium oxide-based transistors with Al_2O_3 gate insulators, inducing spatial distortion in the indium oxide lattice, resulting in the formation of an amorphous film, which reduces interfacial states and suppresses oxygen vacancies. Increasing Yb concentration shifts the V_{th} toward positive values and reduces off-currents from $\approx 10^{-5}$ A to $\approx 10^{-8}$ A, though the off-currents remain relatively high.^[16] Magnesium (Mg) has also been suggested as a dopant to reduce the carrier density in TFTs with indium oxide-based channels, decreasing the field-effect mobility.^[17] In the context of electrolyte-gated transistors (EGTs), as evaluated in this work, chromium (Cr) emerges as a dopant for indium oxide for applications requiring multiple transistors with different threshold voltage values. Although adding Cr could increase the threshold voltage within the evaluated concentrations (0%–12.5%), the threshold voltage remained negative, and the drain current decreased by 60%.^[18] Gallium (Ga) is another interesting dopant for EGTs with indium oxide channels. Because gallium possesses a higher bond dissociation energy with oxygen than indium, it binds more strongly to oxygen. This stronger binding reduces the number of free electrons, increasing the threshold voltage.^[19,20] However, solution-processed indium oxide thin films presented in these studies require calcination temperatures $>200^\circ\text{C}$, which continues to limit the choice of the substrates.

This work focuses on synthesizing indium oxide ($\text{In}_2\text{O}_{3-x}$) and indium gallium oxide (IGO) nanoparticles at varying gallium concentrations. The primary advantage of using nanoparticles lies in their compatibility with additive manufacturing techniques, such as inkjet printing. This compatibility arises from their unique properties, including a large surface area-to-volume ratio, low melting point at the nanoscale, and high diffusion coefficient,^[21,22] which collectively facilitate the curing process at temperatures as low as 100°C , enhancing physical contact between nanoparticles and densification of the printed layer to form a semiconductive thin film.^[23,24] The low-temperature process enables the future fabrication of indium oxide-based microelectronic devices and circuits on flexible substrates like PET and paper. Gallium can substitute indium ions in the crystal lattice with minimal crystal structure disruption since both elements belong to group 13 of the periodic table, have close ionic radii, and exhibit +3 oxidation states. This substitution helps maintain lattice structure and electrical neutrality while preventing various structural defects and impurities in the crystal, particularly oxygen vacancies, thereby enhancing material robustness and durability. Furthermore, gallium is also abundant and cost-effective, making it attractive for the production of large-scale electronic devices.^[25,26]

The nanoparticles are synthesized through a precipitation method and then formulated into a water-based ink. After characterizing the nanoparticles, this ink is used to fabricate EGTs with indium oxide channels at different gallium concentrations, allowing for a thorough investigation of the impact on transistor properties. Specifically, we aim to fine-tune the threshold voltage

of the EGTs to operate in enhancement mode while minimizing drain–source leakage currents. To further emphasize the importance of threshold voltage and leakage currents in microelectronic circuit performance and power consumption, we also fabricate and characterize inverter structures using the optimized EGTs.

2. Results and Discussion

The following study investigates the impact of incorporating Ga^{3+} into $\text{In}_2\text{O}_{3-x}$ by synthesizing and using a water-based ink of IGO nanoparticles. The properties of the printed thin films are evaluated, and their performance in EGTs and inverters is discussed.

2.1. Nanoparticle Synthesis

Indium oxide nanoparticles were synthesized using the precipitation method,^[27] followed by a two-step calcination process. The initial calcination was conducted at 300°C for 1 h, with a subsequent increase in temperature to 650°C for an additional 3 h. Varying concentrations of Ga^{3+} were introduced, specifically 5, 12, 25, 50, and 75 atomic percent (at.%), leading to the samples referred to as IGO-5%, IGO-12%, IGO-25%, IGO-50%, and IGO-75%. Both the nanoparticle powders and the corresponding printed thin films were characterized to study the effects of gallium incorporation on device performance.

X-ray diffraction (XRD) analysis is used to confirm the single-phase structure of the IGO nanoparticles. **Figure 1(a)** shows the XRD peaks for $\text{In}_2\text{O}_{3-x}$ and IGO nanoparticles. The peaks of the indium oxide are well-indexed and match the ICSD-36 970 reference pattern, indicating a cubic bixbyite structure.^[28] Rietveld analysis shows that introducing 5% gallium results in a decrease in the lattice parameter and the unit cell volume, indicating a lattice contraction due to the substitution of gallium within the crystal structure.^[29] Further lattice contraction is observed with the addition of 12% and 25% gallium (**Figure 1(b)**). However, at gallium concentrations of 50% and 75%, no distinct diffraction peaks are observable, indicating an amorphous structure. This amorphous phase is likely attributed to the low calcination temperature, which is insufficient for forming the $\beta\text{-Ga}_2\text{O}_3$ crystal structure.^[30] However, when annealed at 800°C , diffraction peaks begin to emerge, suggesting the onset of crystallization. The corresponding diffraction patterns are presented in **Figure S1**, Supporting Information.

Scanning electron microscopy (SEM) is used to examine the particle size and shape of the synthesized nanoparticles (**Figure 2(a–f)**). Energy-dispersive X-ray spectroscopy (EDX) mapping confirmed the presence and uniform distribution of gallium within the indium oxide (**Figure 2(g–i)**). The identified gallium-to-indium ratios were 5:95, 12:88, 22:78, 49:51, and 71:29 (more results of the EDX spectra are shown in **SI Figure S7**, Supporting Information). **Figure 2(a–f)** displays the SEM images of the IGO nanoparticles, synthesized using the precipitation method. The images show that the particle size ranges from 20–100 nm and increases with gallium concentration. Particle size significantly influences the formulation of nanoparticle inks, studies have shown that nanoparticle size affects ink

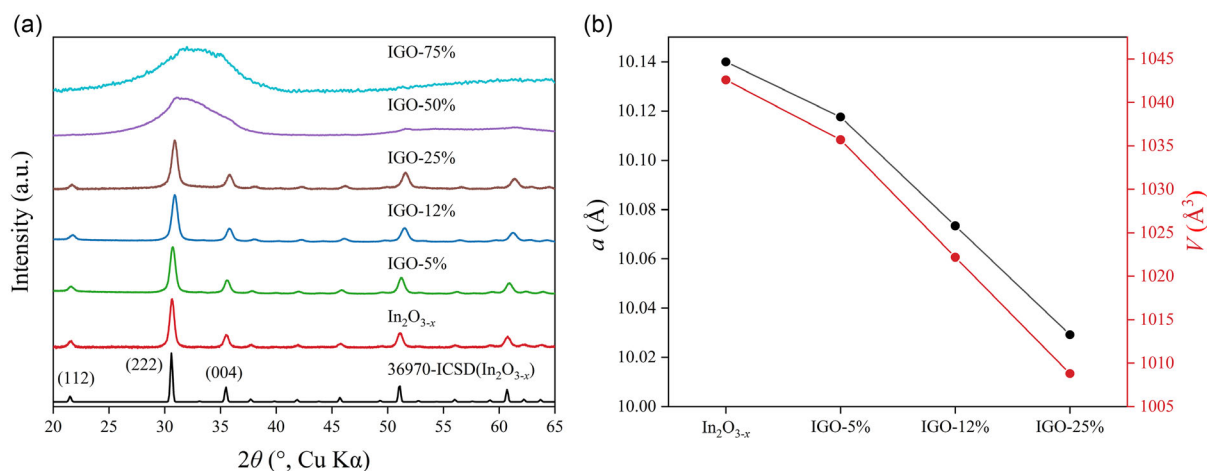


Figure 1. a) XRD patterns and b) lattice parameter α and unit cell volume V of In₂O_{3-x} and IGO nanoparticles.

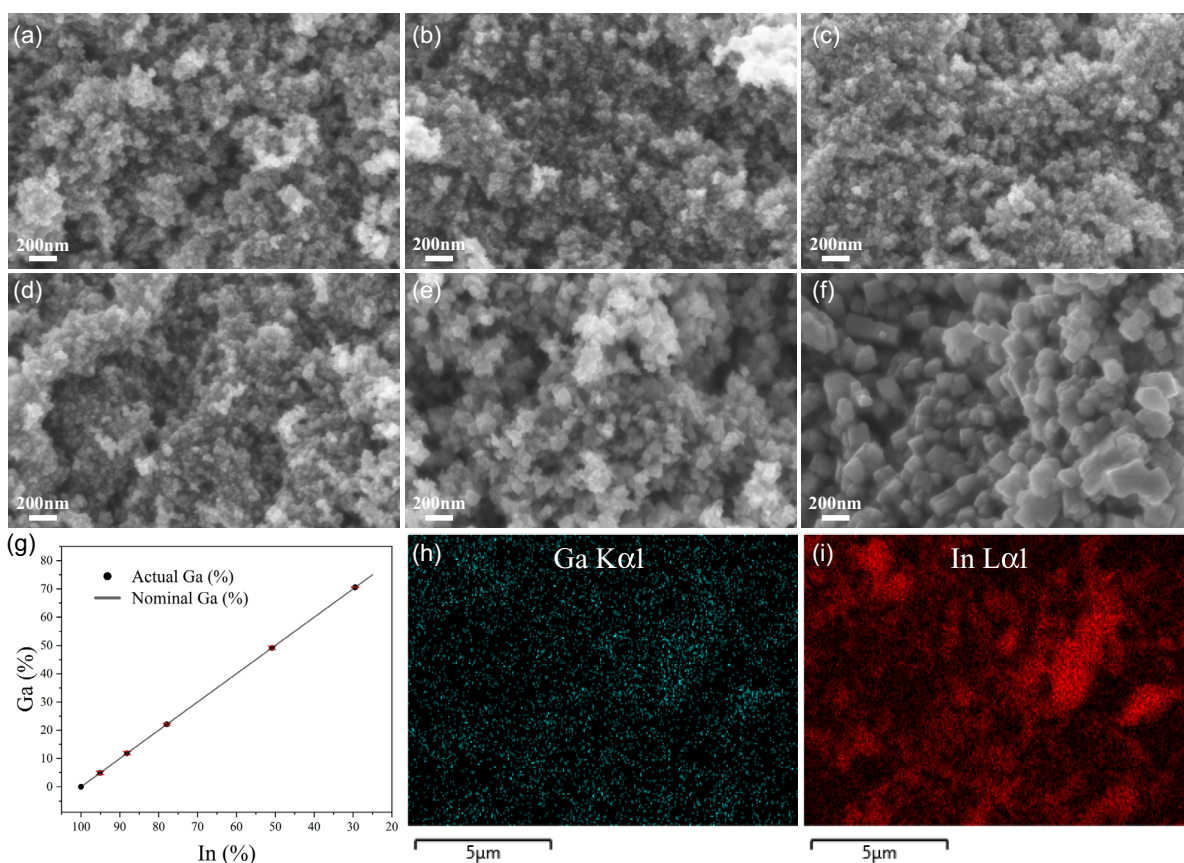


Figure 2. SEM images of synthesized IGO nanoparticles calcined at 650 °C with gallium concentration of a) 0%, b) 5%, c) 12%, d) 25%, e) 50%, and f) 75%. g) Mean value of measured gallium concentration using EDX. h,i) EDX elemental mapping of IGO-5%, showing the distribution of (h) gallium and (i) indium.

rheology and printability.^[31–33] The observed particle sizes in the SEM analysis are suitable for ink formulation, as discussed later. Additionally, a noticeable transformation in particle shape, from spherical to cubic, was observed, particularly at higher gallium concentrations. Although cubic particles can be packed perfectly,

this requires precise alignment, which is not observed in our case. The lack of alignment, combined with the larger particle sizes, led to reduced packing efficiency. Packing efficiency is defined as the spatial distribution of particles, expressed as the ratio of the volume occupied by the nanoparticles to the total

volume of the material. A decrease in packing efficiency negatively impacts the percolative transport of charge carriers, leading to increased scattering, the formation of additional defects, and a reduction in carrier mobility.

At lower magnification, SEM images (Figure S2, Supporting Information) demonstrate a significant decrease in the occurrence of particle aggregates with increasing gallium concentration. This reduction is attributed to changes in the particle morphology and shape caused by the incorporation of gallium. However, these aggregates are broken down during a pearl milling process, which is later required to formulate inks using the synthesized nanoparticles.

Raman spectroscopy was performed to study the oxygen vacancies in the system. **Figure 3** presents the Raman spectra of $\text{In}_2\text{O}_{3-x}$ and IGOs. The Raman spectra of $\text{In}_2\text{O}_{3-x}$ show peaks at 132, 307, 367, 496, and 631 cm^{-1} , characteristic of $\text{In}_2\text{O}_{3-x}$ with a bixbyite structure.^[26,34,35] The similar characteristic Raman spectra are observed for IGO-5%, IGO-12%, and IGO-25%, further confirming that these compositions also possess a cubic bixbyite structure. Each peak corresponds to a distinct vibration in the $\text{In}_2\text{O}_{3-x}$ structure. The peak at 132 cm^{-1} is considered to result from In–O vibration, while the peaks at 307, 496, and 631 cm^{-1} are attributed to the bending and stretching of InO_6 octahedra. Interestingly, the peak at 367 cm^{-1} is associated with the In–O–In vibration mode, which reflects the oxygen vacancies in the system. The intensity of this peak decreases with increasing Ga content, indicating a reduction in oxygen vacancy concentration. The intensities of the other peaks for IGO-5%, IGO-12%, and IGO-25% remain unchanged. In the case of IGO-50%, no characteristic Raman peaks are observed due to its amorphous structure. However, IGO-75 shows slight hints of Raman peaks, which are characteristic of $\beta\text{-Ga}_2\text{O}_3$.^[36]

2.2. Nanoparticle Ink Preparation

To print the synthesized IGO nanoparticles, a water-based nanoparticle ink was formulated using a pearl milling method. Zirconia balls with a diameter of 0.2–0.3 mm were utilized to

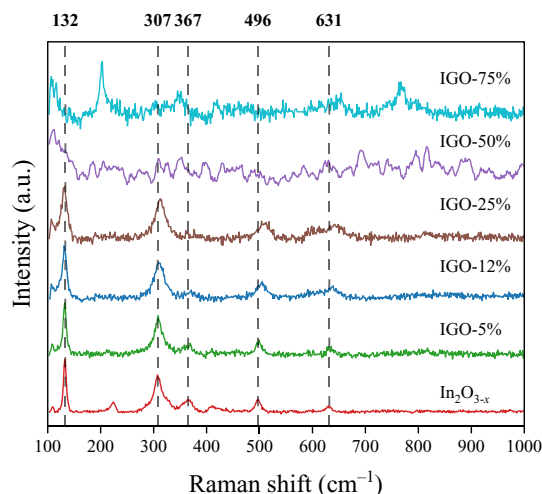


Figure 3. Raman-scattering spectrum of IGO nanoparticles in the range of 100–1000 cm^{-1} for varied gallium concentrations.

break down the nanoparticle aggregates in water. Due to the high surface energy of the nanoparticles, the use of an appropriate stabilizer is crucial. For this purpose, poly (acrylic acid, sodium salt) solution (PaaNa) was selected, as it provides both electrostatic and steric stabilization.^[37,38] More details on ink preparation are available in the Experimental section. Particle dimensions were analyzed using dynamic light scattering (DLS) measurements (Figure S3, Supporting Information), confirming that the particles are in the nanoscale range.

The nanoparticle ink can be printed using various methods, such as inkjet printing, screen printing, and microcontact printing. In this work, a capillary printing method considered a contact printing technique, was selected due to its straightforward functionality. A glass capillary with an $\approx 50\ \mu\text{m}$ opening was used to print the ink between laser-ablated ITO drain–source electrodes, which act as the transistor channel. This was followed by a thermal curing step at 100 $^{\circ}\text{C}$ for 90 min.

Atomic force microscopy (AFM) is used to study the surface morphology, roughness, and particle size of printed thin films. **Figure 4** shows the AFM and SEM images of IGO thin films printed from indium oxide nanoparticle inks with different gallium concentrations. The results indicate a clear trend: both the surface roughness and particle size increase with higher gallium concentrations. For instance, the thin film containing 0% gallium shows a root mean square roughness of $\approx 12\ \text{nm}$, while the root mean square roughness increased to around 24 nm in the thin film with 75% gallium. This increase in surface roughness, along with the previously discussed changes in particle size and morphology, which is noticeable in gallium concentrations of 50% and 75%, significantly impacts the electrical properties of the thin films. Specifically, the increased roughness can enhance charge carrier scattering.^[39] Understanding these variations in surface morphology is crucial, as they directly reflect how introducing gallium influences the structural and electronic properties of the thin films. However, at lower concentrations, the influence of variation in particle size, shape, and roughness is negligible. This insight highlights the importance of fine-tuning nanoparticle composition to optimize the performance of printed thin films in microelectronic devices.

X-ray photoelectron spectroscopy (XPS) is used to confirm the oxidation state of gallium and indium within the printed thin films and to corroborate the formation of cubic indium oxide with the introduction of gallium. **Figure 5a** shows $\text{In } 3d_{3/2}$ and $3d_{5/2}$ core level peaks at ≈ 445 and 452 eV, respectively, indicating that In^{3+} is the dominant oxidation state, demonstrating the formation of indium oxide.^[40] The indium oxide peaks shift to higher binding energies with the introduction of gallium. This is due to the difference between the electronegativities of indium and gallium.^[41] With its higher electronegativity, gallium decreases the electron density around the indium atoms, resulting in increased binding energy. The peak at 1118 eV is related to the Ga^{3+} oxidation state.^[42]

2.3. EGT/Inverter Device Fabrication

To investigate the influence of gallium incorporation on device performance, the indium oxide nanoparticle inks were printed between ITO-laser-structured drain and source electrodes to

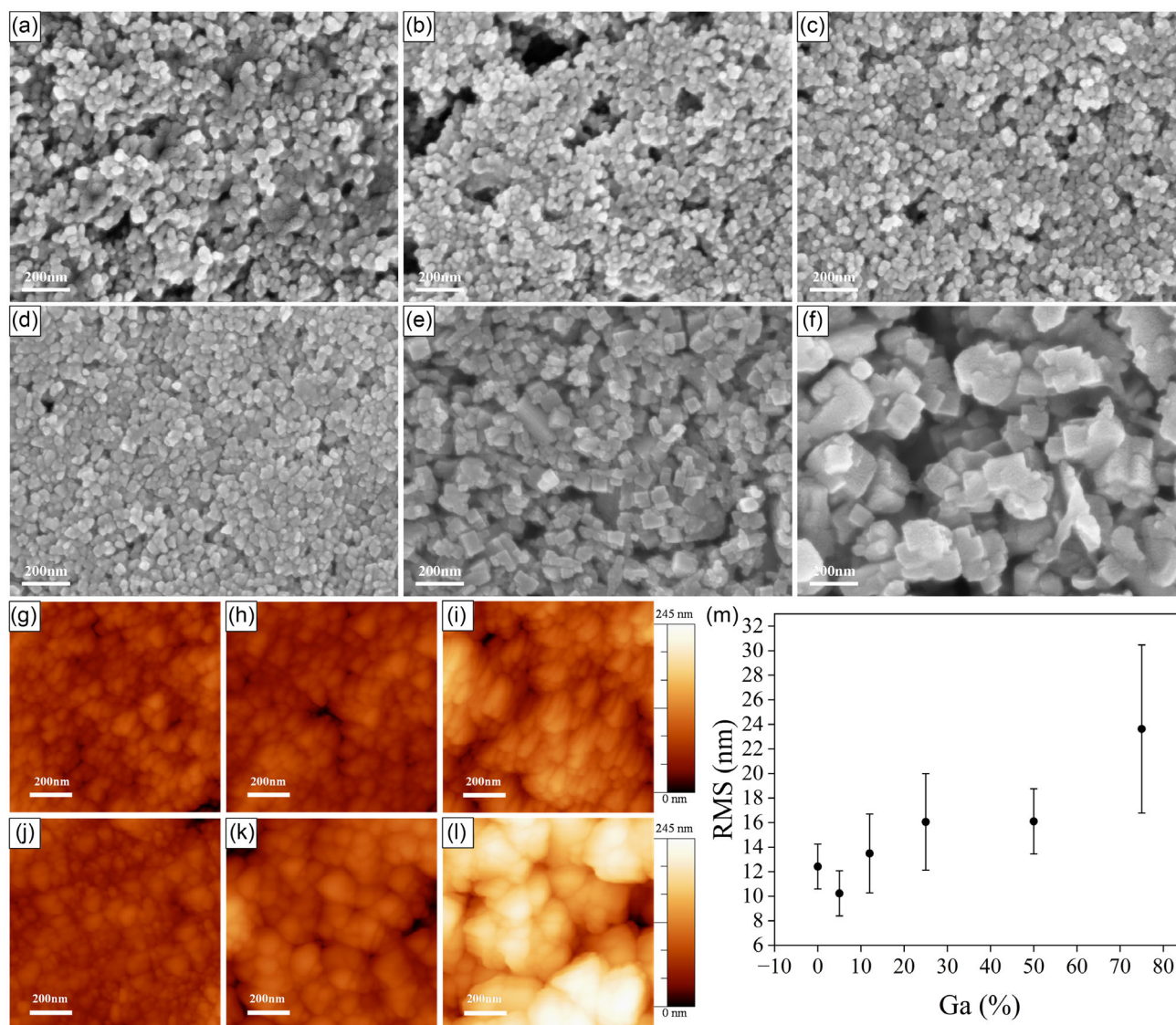


Figure 4. SEM images and AFM height image of IGO capillary-printed thin films with a gallium concentration of a,g) 0%, b,h) 5%, c,i) 12%, d,j) 25%, e,k) 50%, and f,l) 75%. m) Mean values of root mean square (RMS) roughness of IGO capillary-printed thin films at different gallium concentrations.

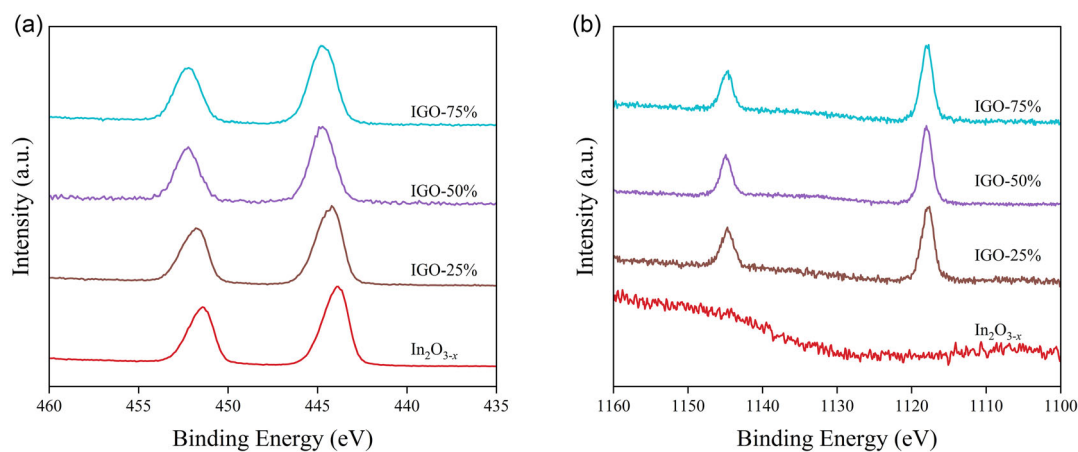


Figure 5. XPS spectra of IGO printed thin films with varied gallium concentration. a) Indium oxide and b) gallium oxide.

fabricate EGTs. The EGTs feature a W/L ratio of 200/50 μm , and a total of 60 EGTs for each gallium concentration, were successfully fabricated and evaluated. A composite solid polymer electrolyte (CSPE) is used as the gate insulator, providing high gate capacitance and thus enabling low operating voltages.^[43] Additionally, PEDOT:PSS is inkjet-printed as the top gate. The EGT stack is shown in **Figure 6a**.

The transfer curves (Figure 6b) show the relationship between the drain-source current (I_{ds}) and the gate-source voltage (V_{gs}) while maintaining a constant drain-source voltage (V_{ds}) of 1 V at different gallium concentrations. The output curves are shown in Figure S4 in the supporting information. The recorded I_{ds} curves constitute the mean value of ≈ 60 EGTs for each gallium concentration, with respective error bars. As the gallium concentration increases, the transfer curves exhibit a rightward shift, indicating a rise in both the onset voltage (V_{on}) and V_{th} . Simultaneously, I_{ds} decreases (Figure 6c), which can be attributed to gallium's stronger binding to oxygen, thereby reducing oxygen vacancies and lowering the carrier density.

At $V_{gs} = 0$ V, the I_{ds} for $\text{In}_2\text{O}_{3-x}$ EGTs were in the microampere range, despite a positive V_{th} , indicating the EGT is still turned on. In contrast, the introduction of gallium results in a significant reduction of I_{ds} , down to values around 10^{-10} A, which is lower

than the values discussed in the introduction,^[16–19] effectively reducing the drain-source leakage currents. This reduction in I_{ds} is advantageous for maintaining the device in the off-state when no voltage is applied to the gate electrode (Figure 6c).

The impact of increasing gallium concentration on the V_{th} is significant. As shown in Figure 6d, V_{th} initially increased from $\text{In}_2\text{O}_{3-x}$ to IGO-12%, then stabilized until IGO-50%. This stability can be attributed to the oxygen vacancies reaching a stable level with the addition of gallium, preventing further reduction and balancing the carrier density. However, a significant rise in V_{th} is observed for IGO-75%, likely due to the formation of an amorphous phase, as previously discussed.

The field-effect mobility (μ_{fet}), calculated from the linear region of the transfer curve (Equation 1), also decreased with gallium incorporation (Figure 6e).

$$\mu_{fet} = \frac{g_m L}{WC_g V_{ds}} \quad (1)$$

where g_m is the transconductance, defined as dI_{ds}/dV_{ds} , and C_g is the gate capacitance, assumed to be $4.33 \times 10^{-6} \text{ F cm}^{-2}$ as extracted from the previous work.^[44] μ_{fet} initially drops from $44.10 \text{ cm}^2/(\text{Vs})$ ($\text{In}_2\text{O}_{3-x}$) to $4.82 \text{ cm}^2/(\text{Vs})$ (IGO-5%), due to the

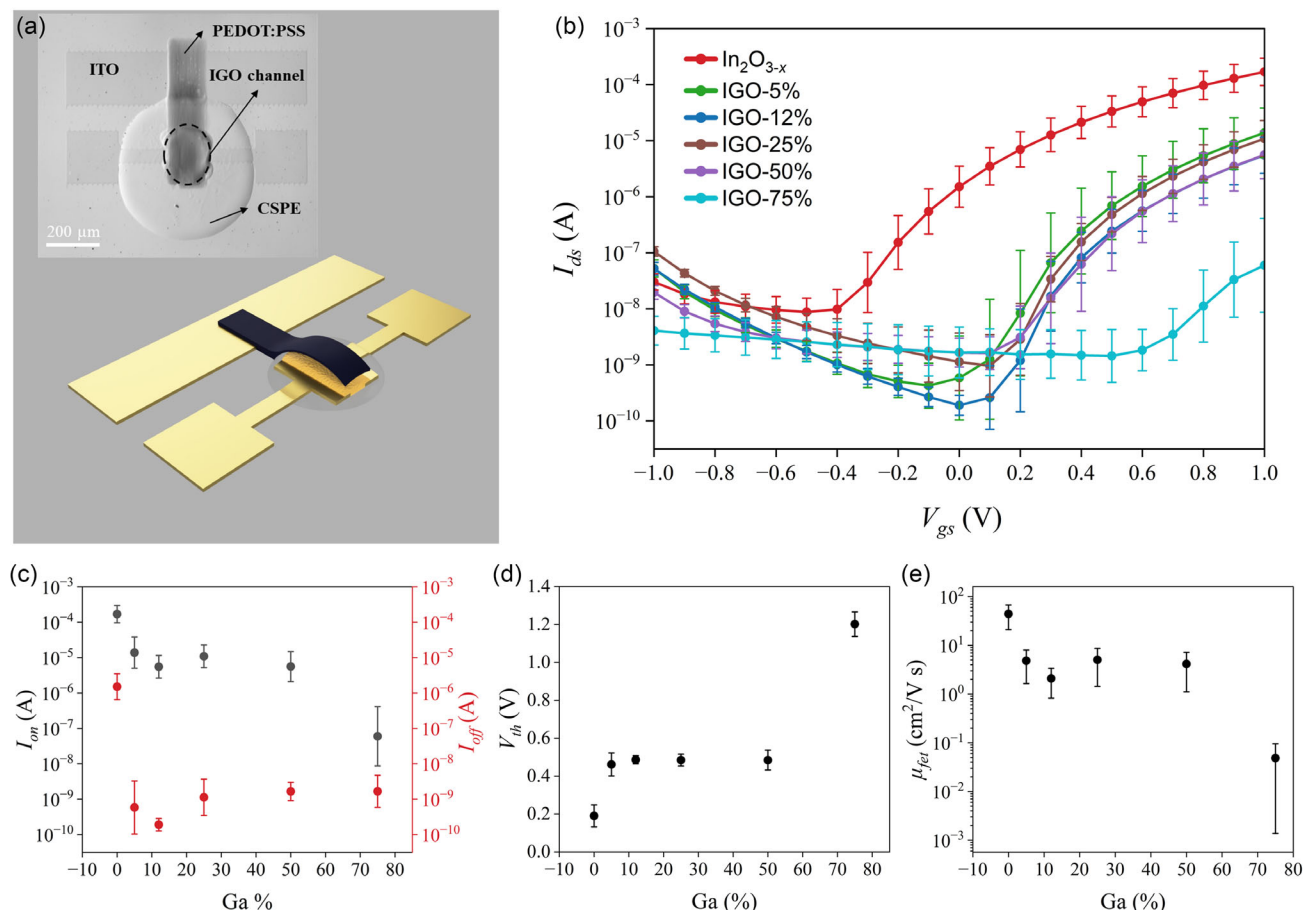


Figure 6. a) Schematic and optical microscopy image of the evaluated printed EGT with an indium oxide nanoparticle-based channel. b) Mean transfer curves of the electrolyte-gated field-effect transistors at different gallium concentrations, measured at a drain-source voltage of 1 V. Mean values of the c) on- and off-currents, d) threshold voltage, and e) mobility of the EGTs with different gallium concentrations.

lower carrier density. Afterward, μ_{fet} remains stable with small fluctuations until IGO-50%. After further increasing the gallium concentration, the mobility drops to $0.05 \text{ cm}^2/(\text{Vs})$ (IGO-75%). As already mentioned, increasing gallium concentration reduces packing efficiency and increases roughness, leading to increased charge carrier scattering. This scattering is considered the main reason for the decreased μ_{fet} in indium oxide thin films with gallium incorporation.

Furthermore, the device's stability over time has been evaluated. To this end, the characteristics of EGTs with IGO-25% channels have been monitored over 1 year, and the devices show negligible changes in threshold voltage, on-, and off-currents (Figure S5, Supporting Information). To assess the device's stability, positive bias stress (PBS), negative bias stress (NBS), and cyclic stability measurements were conducted, demonstrating that the devices are stable under various stress conditions (Figures S8–S11, Supporting Information).

The transfer characteristics of the examined EGTs indicate that the introduction of gallium reduces the drain–source currents at a gate–source voltage of 0 V by three orders of magnitude, which is beneficial for reducing power consumption in digital circuits. Therefore, inverters based on EGTs with $\text{In}_2\text{O}_{3-x}$ and IGO nanoparticles are fabricated and compared. Among the different gallium concentrations, IGO-12% was selected due to the positive V_{th} and lowest drain–source current at 0 V gate–source voltage, while maintaining reasonable on-currents.

The inverters were designed using both transistor-resistor logic (TRL) and transistor-transistor logic (TTL) topologies.^[45] In the TRL topology, a resistor is present in the pull-up network (connection between the supply and the output nodes), while an EGT, operating in enhancement mode, is connected in the

pull-down network (connecting the output and ground nodes). In the TTL topology, an EGT operating in depletion mode is placed in the pull-up network, where its gate electrode is connected to the source electrode, and an enhancement-mode EGT is connected to the pull-down network. The respective gate electrodes of the EGTs in the pull-down network serve as the input of the inverter (Figure 7c,f).

Figure 7 demonstrates the mean values of electrical characteristics obtained from thorough measurements of 30 individual TTL and TRL inverters for both $\text{In}_2\text{O}_{3-x}$ and IGO-12% compositions. This comprehensive dataset emphasizes the reliability and consistency of the observed electrical properties. The TRL inverter topology includes a $250 \text{ k}\Omega$ pull-up resistor and EGTs with $\text{In}_2\text{O}_{3-x}$ and IGO-12% nanoparticle channels as the pull-down EGTs. The transfer curves of the TRL inverter show that the input signals are inverted at the output, with a gain of up to -3 , independent of the presence of gallium. However, in IGO-12%, the input value at which the maximum gain occurs shifts toward $V_{\text{dd}}/2$, where V_{dd} represents the supply voltage. This shift results in more symmetrical voltage characteristics for the inverter and improves the output swing, allowing a high state closer to the supply voltage. This improvement is further confirmed by the transient analysis of the inverter, where a voltage pulse between 0 V and 1 V with a frequency of 1 Hz is applied (Figure 8a). However, the output voltage of the TRL inverters with an IGO-12% EGT is not completely pulled down, which could be solved by further increasing the resistor in the pull-up network. Increasing the resistor would reduce the speed of the inverter and increase the area overhead.

With the help of the TTL topology, the output swing of the inverter can be reduced without sacrificing speed or increasing

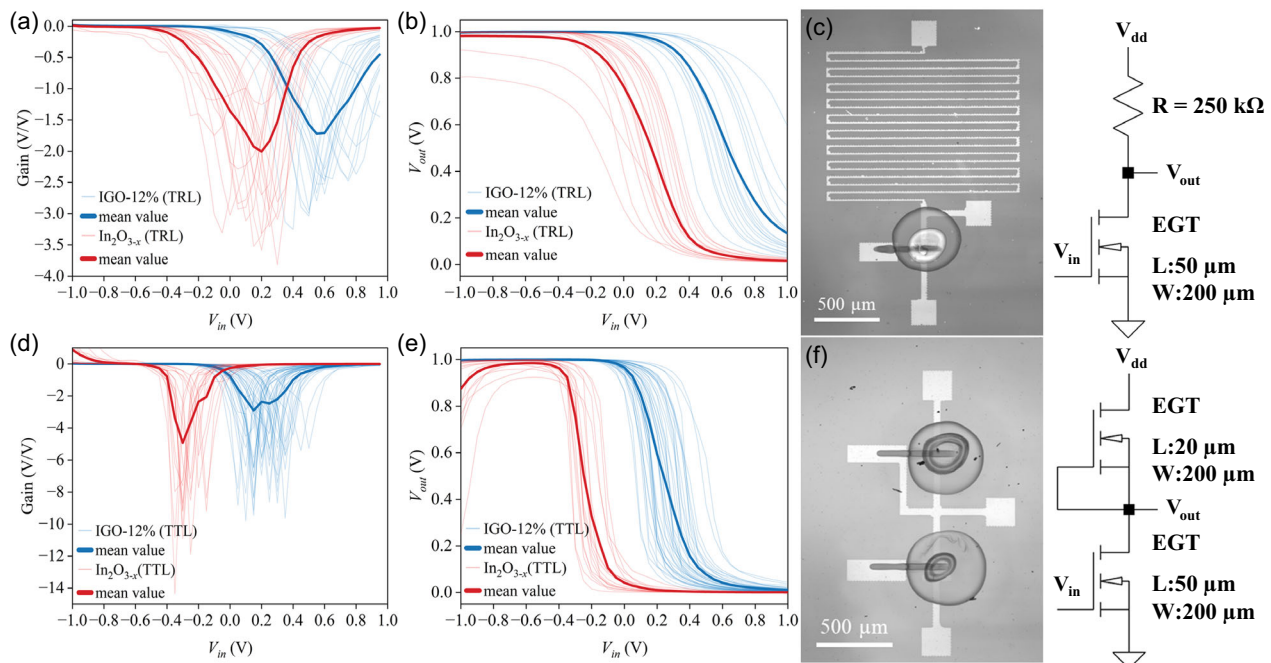


Figure 7. Inverter characteristics of a–c) transistor/resistor inverter design (TRL), (a) output gain diagram, (b) voltage transfer curve, and (c) microscopic image and schematic of TRL designed inverter. d–f) Transistor/transistor inverter design (TTL), (d) output gain diagram, (e) voltage transfer curve, and (f) microscopic image and schematic of TTL designed inverter.

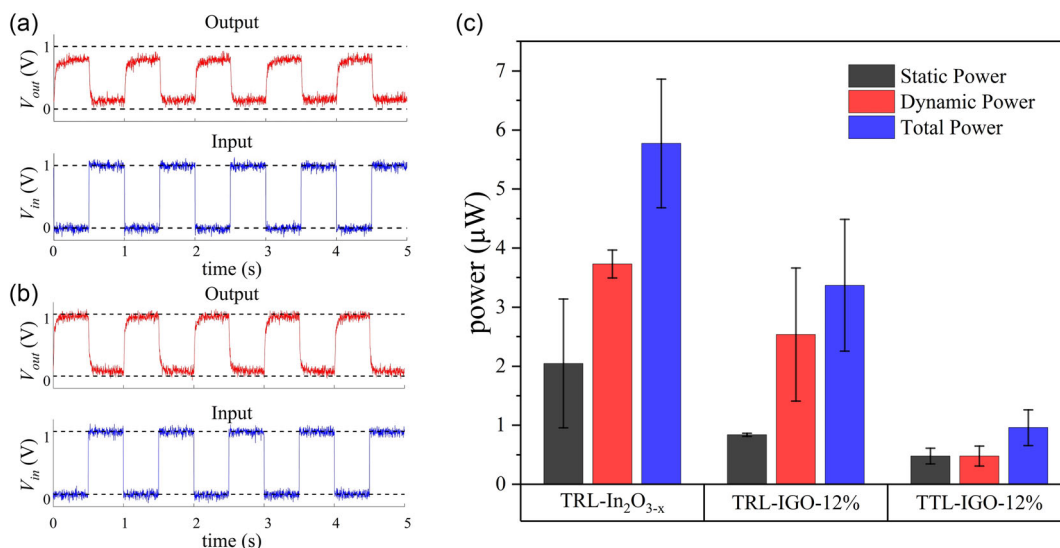


Figure 8. Transient measurement of a) IGO-12% TRL inverter, b) IGO-12% TTL inverter at a supply voltage of 1 V, c) power consumption of TRL and TTL designed inverter at different supply voltage levels for In₂O_{3-x} and IGO-12%.

the area. In addition, the TTL topology consumes less power, as the EGT in the pull-up network can be switched on and off. However, it is necessary to use an enhancement-mode EGT with positive V_{th} ; otherwise, the inverter switches at negative input voltages (mean value -0.3 V) (Figure 7d), as shown by the red curves in Figure 7e. In digital circuits, this would require an additional power supply, increasing the complexity of the circuits. To avoid this, the EGT in the pull-up network needs to operate in depletion mode. Based on the previous EGT characteristics, IGO-12% EGT is used in the pull-down network, and an In₂O_{3-x} EGT is used in the pull-up network. By incorporating gallium in the channel of the pull-down EGT, the inverters switch at a mean input voltage of around 0.2 V (Figure 7e, blue curve), demonstrating that it is necessary to introduce gallium to the channel of the pull-down EGT. Moreover, the TTL topology shows a higher gain of up to -9 , compared to the TRL logic (Figure 7d).

By comparing the transient analysis of the TRL and TTL inverters (Figure 8a and b), it is evident that the TTL topology shows a full voltage swing, whereas the TRL topology does not. Additionally, the TTL topology exhibits a propagation delay time (the time that an input signal is required to propagate from the input to the output) of around 9.5 ms, compared to 11.3 ms for the TRL topology, indicating that the TTL topology is faster.

Regarding power consumption (Figure 8c), using IGO-12% reduces static power consumption which leads to a significant decrease in overall power consumption in TRL. This reduction is primarily due to decreased drain-source leakage currents. Moreover, adopting the TTL topology further decreases the power consumption, particularly in terms of dynamic power consumption, due to the switchable active load. While the change in static power consumption is negligible, the reduction in dynamic power consumption results in an overall decrease in power consumption. Therefore, the TTL topology is more energy-efficient and preferable to the TRL topology.

In the past, fabricating TTL topology logic gates with EGTs using indium oxide channels required adjusting the channel length, as the channel length directly influences the conductivity of the EGT. Consequently, the V_{th} of the EGT is influenced to some extent by the channel length. For this reason, the pull-up EGT required a narrow channel length (≈ 10 μm), while the EGT in the pull-down network was designed with a wider channel length (≈ 100 μm).^[45] With the presented gallium incorporation approach, the channel geometry of the EGTs can be maintained within a range compatible with most additive manufacturing techniques. Moreover, the maximum curing temperature, reduced to 100 °C due to the use of nanoparticles, enables the possibility of printing microelectronic circuits on various flexible substrates in the future.

3. Conclusion

In this work, indium oxide nanoparticles incorporated with gallium were successfully synthesized and formulated into a water-based ink, enabling their application as channel materials in printed electronic devices without the use of toxic solvents. The printed-nanoparticle thin films demonstrated effective curing at low temperatures (100 °C), significantly enhancing their suitability for environmentally friendly fabrication and compatibility with established printed electronics processes and materials. By adjusting the gallium concentration in the electrolyte-gated transistors, the threshold voltage and drain-source leakage currents were effectively tuned. Specifically, at a gallium concentration of 12%, the threshold voltage shifted from ≈ 0.20 V to around 0.35 V, while the drain-source leakage currents were reduced by three orders of magnitude. These improvements are advantageous for lowering the power consumption in microelectronic circuits, highlighting the potential of gallium-incorporated indium oxide nanoparticles for future applications.

4. Experimental Section

Materials: Indium (III) nitrate hydrate, (99.999% trace metals basis, Sigma-Aldrich), gallium (III) nitrate hydrate (crystals, and lumps, 99.999% trace metals basis, Sigma-Aldrich), and ammonium hydroxide (28%–32% NH₃ basis, GPR RECTAPUR) were used to synthesize IGO nanoparticles. Yttria-stabilized zirconia (YSZ) grinding media, 0.2–0.3 mm beads (Inframat Advanced Materials), and Poly(acrylic acid, sodium salt) solution (Mw ≈ 15 000, 35 wt% in H₂O, Sigma Aldrich) were used to produce the nanoparticle ink.

Propylene carbonate (anhydrous, 99.7%) (PC), poly(vinyl alcohol) (average Mw 13 000–23 000, 98% hydrolyzed) (PVA), dimethyl sulfoxide (anhydrous, ≥99.9%) (DMSO), and lithium perchlorate (99.99% trace metals basis) (LP), all purchased from Sigma-Aldrich, were used to prepare the composite solid polymer electrolyte (CSPE) used as a dielectric in the EGTs and inverters.

Poly(3,4-ethylenedioxythiophene)-poly(styrene sulfonate) (PEDOT:PSS, 3.0–4.0% in H₂O, high-conductivity grade, Sigma-Aldrich) and ethylene glycol (1,2-Ethandiol, glycol, Sigma-Aldrich) were used as the top-gate material for the EGTs and inverters.

ITO-coated glass substrate (1.1 mm thickness, $R < 30 \Omega$, purchased from Präzisions Glass & Optic GmbH) was used.

Methods: IGO Nanoparticle Synthesis: IGO nanoparticle powder with different gallium concentrations was synthesized using the precipitation method. 0.1 M solutions of indium nitrate and gallium nitrate precursors were mixed in different ratios of 100:0, 95:5, 88:12, 75:25, 50:50, and 25:75 during stirring. After 2 h of stirring and 1 h of sonication, the solution was heated up to 70 °C, and 2.5% of Ammonia solution was added to the solution drop by drop until the pH reached 10 to obtain indium gallium hydroxide precipitation. The precipitated solution was stirred for an additional 2 h and aged overnight. The precipitates were collected using a Hettich Universal 320 centrifuge at 7000 rpm for 5 min and dried overnight at 80 °C. The dried powders were thoroughly ground and calcined in two steps to get IGO nanoparticles. First powders were heated up to 300 °C for 1 h and then the temperature was increased at a ramp rate of 5 °C per minute to 650 °C for an additional 3 h. The final products were ground and used for preparing IGO ink.

IGO Nanoparticle Ink Preparation: The pearl milling process^[38] The pearl milling process was carried out to produce a water-based nanoparticle ink. First, yttria-stabilized zirconia (YSZ) grinding media, double-distilled water, synthesized IGO nanoparticles, and a poly(acrylic acid, sodium salt) solution as a surfactant were added to a glass beaker, which was then covered with a rotator cap. The mixture was subsequently pearl-milled for 90 min at a speed of 5000 rpm. The resulting nanoparticle ink was filtered through PVDF filters with pore sizes of 2.7, 1.2, 0.7, and 0.45 μm, respectively. Just before printing, 20 mM NaCl was added to the ink to remove the surfactant, allowing the nanoparticles to reaggregate and form a thin film. The synthesized nanoparticle powders and inks, as shown in Figure S6, Supporting Information, exhibited a color transition from yellowish to whitish with increasing gallium concentration.

PEDOT:PSS and CSPE Ink Preparation: PEDOT:PSS and CSPE ink were prepared using the recipe from previous work.^[9] Briefly, Poly(3,4-ethylenedioxythiophene)-poly(styrene sulfonate) (3.0–4.0% in H₂O) was mixed with 4 wt% ethylene glycol. The solution was stirred for 60 min at room temperature, followed by filtration through a 0.45 μm PVDF filter. CSPE was prepared by dissolving 0.3 grams of PVA in 9 grams of DMSO at 90 °C and 0.07 grams of lithium perchlorate (LP) in 0.63 grams of propylene carbonate (PC) at room temperature for 2 h. Afterward, two prepared mixtures were combined and stirred overnight, followed by filtration through a 0.2 μm PTFE filter.

Printing Process: The NLP 2000 nanolithography: The NLP 2000 nanolithography system (NanoInk, USA) was used for contact printing^[46] of In₂O_{3-x} and IGO nanoparticle inks as the device channels, utilizing a mounted glass capillary with an approximate 50 μm opening at its tip. The printed channels were cured at 100 °C for 90 min. Afterward, a Dimatix 2831 inkjet printer was used to print the CSPE ink as a dielectric, which was then cured at 50 °C, followed by printing of PEDOT:PSS as a top gate.

Scanning Electron Microscopy (SEM) and Energy-Dispersive X-Ray Spectroscopy (EDX): To study the morph: To study the morphology of the synthesized IGO nanoparticles SEM LEO-1530 Zeiss was used with an acceleration voltage of 5 kV and a working distance of 5.2 mm. In addition, dispersity and concentration of indium and gallium were measured by mapping from multiple regions of the samples, each with dimensions of 10.8 by 14.4 μm, using an EDX detector (Oxford Instruments) with an acceleration voltage of 20 kV and a working distance of 8.5 mm.

Atomic Force Microscopy (AFM): An atomic force microscope (AFM) from Bruker Dimension: An atomic force microscope (AFM) from Bruker Dimens Icon was used to study the morphology and roughness of the printed thin films. Tap 300 Al-G Budget Sensors probes were employed in tapping mode. WSxM software^[47] was used to analyze and calculate the thin-film roughness. No flattening was applied to the AFM images.

X-Ray Photoelectron Spectroscopy (XPS): X-ray photoemission spectra were collected by irradiating the sample with an Al-Kα X-Ray source (1486.6 eV). The X-rays for XPS were generated by an Omicron XM1000 MkII at an operating power of 300 W. The resultant electrons from the irradiated sample were detected using a SPECS Phoebias 150 spectrometer positioned directly above the sample.

Optical Microscopy: Nikon Eclipse 80i upright microscope (Ni: Nikon Eclipse 80i upright microscope (Nikon, Japan) equipped with a Nikon DS-Qi2 camera (Nikon, Germany) was used to capture optical images of printed EGTs and inverters, which were analyzed by NIS-Elements imaging software.

Raman Spectroscopy: A Renishaw in-via confocal micr: A Renishaw in-via confocal microscope was used to measure the Raman spectroscopy. The Raman spectra were collected at a magnification of 100X with a green laser (532 nm). The spectra were collected from 1000–100 cm^{−1} for 30 s and with 10 accumulations at a laser power of 5%.

X-Ray Diffraction Analysis: In this study, X-Ray diffraction (XRD) measurements were conducted using a Bruker D8 Advance X-Ray diffractometer equipped with a Cu Kα radiation source ($\lambda = 1.5418 \text{ \AA}$) and a LynxEye detector. The powder samples of synthesized IGO nanoparticles were used for the measurement. The XRD patterns were recorded in the 2θ range of 10°–80° with a step size of 0.02° and a scan speed of 1.5 s per step. All measurements were performed in an ambient environment. The XRD data were analyzed using HighScore Plus (Malvern Panalytical) and Origin Pro software with reference patterns obtained from the Inorganic Crystal Structure Database (ICSD). Rietveld analysis was performed by using TOPAS Academics V5 software. The refinement was done with modifications to the elements and their proportion used in the respective samples. The instrumental intensity distribution was determined by employing a reference scan of SRM-1976b (strain-free Al₂O₃ in a glassy matrix, particle size >2 μm, random orientation).

Electrical Characterization: All electrical characterizations in this research were performed using a SÜSS MicroTec probe station and EasyEXPERT software. The performance of EGTs and inverters was measured with an Agilent 4156c Precision Semiconductor Parameter Analyzer. Additionally, transient and power consumption measurements of the printed inverters were conducted using a Keithley 3390 Arbitrary Waveform Generator, a Yokogawa DL6104 Digital Oscilloscope, and LabVIEW software. All data were analyzed using MATLAB and Origin Pro.

Supporting Information

Supporting Information is available from the Wiley Online Library or from the author.

Acknowledgements

This research was funded by the Deutsche Forschungsgemeinschaft (DFG, German Research Foundation) under Germany's Excellence Strategy via the Excellence Cluster "3D Matter Made to Order" (EXC-2082/1-390761711). It has also been supported by the Carl Zeiss

Foundation through the “Carl-Zeiss-Foundation-Focus@HEiKA”, the State of Baden-Württemberg, and the Karlsruhe Institute of Technology (KIT). This work was partly carried out with the support of the Karlsruhe Nano Micro Facility (KNMF, www.knmf.kit.edu), a Helmholtz Research Infrastructure at the Karlsruhe Institute of Technology (KIT, www.kit.edu). J.A.-H., B.B., and S.S. acknowledge financial support from the KIT via the project Auto.MAP and the Helmholtz Program “Materials Systems Engineering” under program no. 43.31.01.

Open Access funding enabled and organized by Projekt DEAL.

Conflict of Interest

The authors declare no conflict of interest.

Data Availability Statement

The data that support the findings of this study are openly available in Radar4KIT at <https://doi.org/10.35097/n8tectc1s03w275y>, reference number 20250417.

Keywords

additive manufacturing, electrolyte-gated field-effect transistors, indium oxide, metal oxide semiconductors, printed electronics

Received: April 17, 2025

Revised: May 15, 2025

Published online:

- [1] P. Barquinha, R. Martins, L. Pereira, E. Fortunato, *Transparent Oxide Electronics: From Materials To Devices*, Wiley, United Kingdom **2012**.
- [2] A. Charnas, Z. Zhang, Z. Lin, D. Zheng, J. Zhang, M. Si, P. D. Ye, *Adv. Mater.* **2024**, 36, 2304044.
- [3] J. H. Noh, S. Y. Ryu, S. J. Jo, C. S. Kim, S.-W. Sohn, P. D. Rack, D.-J. Kim, H. K. Baik, *IEEE Electron Device Lett.* **2010**, 31, 567.
- [4] N. Xiao, S. Yuvaraja, D. Chettri, Z. Liu, Y. Lu, C. Liao, X. Tang, X. Li, *J. Phys. Appl. Phys.* **2023**, 56, 425102.
- [5] L.-Y. Ma, N. Soin, S. N. Aidit, F. A. Md Rezali, S. F. Wan Muhamad Hatta, *Mater. Sci. Semicond. Process.* **2023**, 165, 107658.
- [6] J. Leppaniemi, K. Eiroma, H. S. Majumdar, A. Alastalo, *IEEE Electron Device Lett.* **2016**, 37, 445.
- [7] Z. Chen, X. Z. Wu, T. Zhou, Z. Cui, *The 9th IEEE Inter. Conf. on Nano/ Micro Engineered and Molecular Systems (NEMS)*, IEEE, Honolulu, Hawaii, USA **2014**.
- [8] S. Chung, K. Cho, T. Lee, *Adv. Sci.* **2019**, 6, 1801445.
- [9] G. Cadilha Marques, L. Yang, Y. Liu, V. Wollerssen, T. Scherer, B. Breitung, M. Wegener, J. Aghassi-Hagmann, *Adv. Mater. Technol.* **2023**, 8, 2300893.
- [10] F. Gunkel, D. V. Christensen, Y. Z. Chen, N. Pryds, *Appl. Phys. Lett.* **2020**, 116, 120505.
- [11] Z. Zang, W. Cai, Y. Zhou, *Metal Oxide Semiconductors: Synthesis, Properties, And Devices*, Wiley, Weinheim, Germany **2024**.
- [12] J. H. Bae, J. H. Lee, S. P. Park, T. S. Jung, H. J. Kim, D. Kim, S.-W. Lee, K.-S. Park, S. Yoon, I. Kang, H. J. Kim, *ACS Appl. Mater. Interfaces* **2020**, 12, 38350.
- [13] W. Cai, M. Li, H. Li, Q. Qian, Z. Zang, *Appl. Phys. Lett.* **2022**, 121, 062108.
- [14] H. Oh, J.-Y. Oh, C. W. Park, J.-E. Pi, J.-H. Yang, C.-S. Hwang, *Nat. Commun.* **2022**, 13, 4963.
- [15] H.-L. Zhao, F. Shan, X.-L. Wang, G. Tarsoly, J.-Y. Lee, S.-J. Kim, *IEEE Trans. Electron Devices* **2023**, 70, 6354.
- [16] Z. Wang, T. Zhao, J. Li, J. Zhang, *IEEE Trans. Electron Devices* **2023**, 70, 1073.
- [17] F. Schöppach, D. Splith, H. Von Wenckstern, M. Grundmann, *Adv. Electron. Mater.* **2023**, 9, 2300291.
- [18] F. Neuper, A. Chandresh, S. A. Singaraju, J. Aghassi-Hagmann, H. Hahn, B. Breitung, *ACS Omega* **2019**, 4, 20579.
- [19] J. R. Pradhan, M. Singh, S. Dasgupta, *Adv. Electron. Mater.* **2022**, 8, 2200528.
- [20] Y. G. Kim, T. Kim, C. Avis, S.-H. Lee, J. Jang, *IEEE Trans. Electron Devices* **2016**, 63, 1078.
- [21] J. Yan, *Nanomaterials* **2021**, 11, 927.
- [22] N. Eom, M. E. Messing, J. Johansson, K. Deppert, *J. Phys. Chem. C* **2021**, 125, 16220.
- [23] Z. Z. Fang, H. Wang, *Int. Mater. Rev.* **2008**, 53, 326.
- [24] J. R. Greer, R. A. Street, *Acta Mater.* **2007**, 55, 6345.
- [25] J. H. Lim, S. M. Lee, H.-S. Kim, H. Y. Kim, J. Park, S.-B. Jung, G. C. Park, J. Kim, J. Joo, *Sci. Rep.* **2017**, 7, 41992.
- [26] J. A. Ramos-Ramón, U. Pal, A. Cremades, D. Maestre, *Appl. Surf. Sci.* **2018**, 439, 1010.
- [27] M. Seetha, S. Bharathi, A. Dhayal Raj, D. Mangalaraj, D. Nataraj, *Mater. Charact.* **2009**, 60, 1578.
- [28] H. Ullah, Z. H. Yamani, A. Qurashi, J. Iqbal, K. Safeen, *J. Mater. Sci. Mater. Electron.* **2020**, 31, 17474.
- [29] H. J. Chun, Y. S. Choi, S. Y. Bae, H. C. Choi, J. Park, *Appl. Phys. Lett.* **2004**, 85, 461.
- [30] S. Paul, T.-S. Chen, M.-P. Houg, J. V. Li, *AIP Adv.* **2022**, 12, 055314.
- [31] H.-J. Park, K. Ryu, H.-L. Lee, Y.-J. Moon, J. Y. Hwang, S. J. Moon, *Materials* **2024**, 17, 978.
- [32] A. Mavuri, A. G. Mayes, M. S. Alexander, *Materials* **2019**, 12, 2277.
- [33] Y. T. He, J. Wan, T. Tokunaga, *J. Nanoparticle Res.* **2008**, 10, 321.
- [34] F. Saeed, A. Farooq, A. Ali, S. Mehmood, C. Cepek, S. Bhardwaj, A. Ul-Hamid, A. S. Bhatti, *Mater. Sci. Eng. B* **2020**, 262, 114781.
- [35] D. Deng, Y. Wang, J. Jiang, Y. Bai, Y. Chen, H. Zheng, H. Ou, Y. Lei, *Chem. Commun.* **2024**, 60, 9364.
- [36] I. López, A. D. Utrilla, E. Nogales, B. Méndez, J. Piqueras, A. Peché, J. Ramírez-Castellanos, J. M. González-Calbet, *J. Phys. Chem. C* **2012**, 116, 3935.
- [37] X. Liu, Q. Chen, K. Xu, W. Zhang, P. Wang, *J. Appl. Polym. Sci.* **2009**, 113, 2693.
- [38] T. T. Baby, S. K. Garlapati, S. Dehm, M. Häming, R. Kruk, H. Hahn, S. Dasgupta, *ACS Nano* **2015**, 9, 3075.
- [39] X. Wang, A. Dodabalapur, *J. Appl. Phys.* **2021**, 130, 145302.
- [40] S. Sundaresh, S. D. Nehate, K. B. Sundaram, *ECS J. Solid State Sci. Technol.* **2021**, 10, 065016.
- [41] Z.-Y. Chen, W.-Z. Shao, W.-J. Li, X.-Y. Sun, L. Zhen, Y. Li, *ACS Appl. Nano Mater.* **2022**, 5, 10809.
- [42] C.-H. Choi, Y.-W. Su, L.-Y. Lin, C.-C. Cheng, C. Chang, *RSC Adv.* **2015**, 5, 93779.
- [43] X. Feng, G. C. Marques, F. Rasheed, M. B. Tahoori, J. Aghassi-Hagmann, *IEEE Trans. Electron Devices* **2019**, 66, 5272.
- [44] S. K. Garlapati, N. Mishra, S. Dehm, R. Hahn, R. Kruk, H. Hahn, S. Dasgupta, *ACS Appl. Mater. Interfaces* **2013**, 5, 11498.
- [45] G. C. Marques, A. Birla, A. Arnal, S. Dehm, E. Ramon, M. B. Tahoori, J. Aghassi-Hagmann, *IEEE Trans. Electron Devices* **2020**, 67, 3146.
- [46] N. Hussain, T. Fu, G. Marques, C. Das, T. Scherer, U. Bog, L. Berner, I. Wacker, R. R. Schröder, J. Aghassi-Hagmann, M. Hirtz, *Adv. Mater. Technol.* **2021**, 6, 2100650.
- [47] I. Horcas, R. Fernández, J. M. Gómez-Rodríguez, J. Colchero, J. Gómez-Herrero, A. M. Baro, *Rev. Sci. Instrum.* **2007**, 78, 013705.